Structural Optimisation and Behaviour of the Breakwater Integrated Oscillating Water Column Device

A combined 3D CFD and Structural Analysis

Bart Goeijenbier[1], Jeremy Bricker[2], Alessandro Antonini[3], Giovanni Malara[4], Max A.N. Hendriks[5], Herbert van der Ham[6]

Abstract

The Oscillating Water Column (OWC) device is a relatively young and underdeveloped technology for generating electricity from wave energy. Compared to other common renewable sources such as solar and wind energy, the costs for bottom-standing OWCs are too high for the technology to be economically competitive. A first step in lowering the cost was the integration of OWC devices into breakwaters. Often, OWCs are built quite robustly due to insufficient confidence in the magnitude of the extreme loads. This leaves room for optimisation, which so far has not been looked into in detail. In an attempt to lower the costs further, the possibilities for structural optimisation are investigated in this research. The U-OWC device in Civitavecchia, an OWC with an additional vertical duct, is used as a case study and is modelled in 3D in a one-way coupled hydraulic-structural numerical model. The model contained both a fluid domain, i.e. the wave tank, and a solid domain, i.e. the OWC structure. Coupling the two gives direct feedback on the wave impact in terms of a stress state in the structure. By converting the stresses to sectional forces, a new minimally required wall thickness can be found. Comparing these to the original thicknesses of the three main walls gives the optimisation potential of the OWC structure. Numerical simulations were carried out in operational and design conditions for varying geometries. Based on this, it was found the OWC walls could have been built using 35% less concrete on average. The results also led to a new insight on the structural behaviour. Clear trends were found in where and when to expect critical loads. It was also found that the geometrical changes barely had any influence on these properties. These findings were used to develop a new and simple design method, making a full structural analysis redundant. Removing the structural domain and making use of the found property that water pressures are constant over the transverse width, imply that a 2D model would be sufficient for preliminary design purposes, reducing the model size drastically.

[1]bartgoei@gmail.com, Delft University of Technology, Delft, The Netherlands
[2]J.D.Bricker@tudelft.nl, Delft University of Technology, Delft, The Netherlands and Dept. of Civil & Environmental Engineering, University of Michigan, Ann Arbor, MI, USA
[3]A.Antonini@tudelft.nl, Delft University of Technology, Delft, The Netherlands
[4]giovanni.malara@unirc.it, Mediterranea University of Reggio Calabria, Reggio Calabria, Italy
[5]M.A.N.Hendriks@tudelft.nl, Delft University of Technology, Delft, The Netherlands and Norwegian University of Science and Technology (NTNU), Trondheim, Norway
[6]H.W.M.vanderHam@tudelft.nl, Delft University of Technology, Delft, The Netherlands

Keywords

U-OWC, oscillating water column, structural optimisation, numerical modelling, CFD, FEA

1   Introduction

Wave energy yields a large potential as a source for renewable energy (Gunn and Stock-Williams, 2012; Mørk et al., 2010), but technologies are relatively young, especially when compared to wind and solar energy (WEC, 2016). This is reflected in the respective high values of the Levelised Cost of Energy (LCOE). It represents the economic competitiveness and is defined as the price at which generated electricity should be sold to break even the project over its service lifetime (NEA et al., 2015). Wave energy is characterised by values around 0.5 to 0.6 EUR/kWh, while this is around 0.1 EUR/kWh for sources like wind and solar energy (Magagna and Uihlein, 2015). Lowering the LCOE results in more commercial interest, making wave energy a more viable alternative.

One of the main technologies in wave energy is the Oscillating Water Column (OWC) device. It uses an enclosed water column excited by wave action to generate an airflow through a turbine, which in turn drives a generator. Waves enter the chamber from below and make the water column rise. This forces air out of the chamber and through the turbine, while a falling column causes a reversed airflow. By making use of Wells turbines, electricity is generated from airflow in both directions. A large step in developing the OWC was integrating it into breakwaters. Advantages to singular devices are split costs, easy access and higher energy intensity in front of the chamber. Added costs to the original breakwater design generally are limited to 5 – 10% (Vicinanza et al., 2019). Realised breakwater integrated devices are found in Japan, Spain and Italy.

In an attempt of optimising the device, the hydrodynamic behaviour is already widely researched. Analytical descriptions of the dynamic behaviour may (among others) be found in Boccotti (2007a) and Malara and Arena (2013). Ideally, the eigenperiod of the oscillatory motion of the water column matches that of the predominant incident waves, so the resonance condition is met. The U-OWC, introduced by Boccotti (2007a), yields a different inlet shape with an additional wall and therefore has a larger eigenperiod by default. This gives an advantage over the conventional design (Boccotti, 2007b). A full-scale CFD simulation of the U-OWC device in Civitavecchia, Italy was carried out by Scarpetta et al. (2017), where based on simulated streamlines, they found the geometrical design may still be optimised. The alternative method to lower the LCOE is reduction of the overall costs, where attention is given here to structural costs. Structural optimisation is seen as a viable method to achieve this (Bull and Ochs, 2013; Magagna and Uihlein, 2015). Analysis towards cost distribution showed that a large fraction of the total costs is related to the structure for wave energy in general (OCEAN, 2013). A case study for a breakwater integrated U-OWC showed a value of 75% structural costs (Naty et al., 2016).

Research towards the structural aspects of the OWC is scarce. Rivero (2018) analysed the (wave) pressure distribution along OWC walls for varying geometries with help of numerical models. The pressures were then used as input for a structural analysis in 2D. The addition of the wall in the U-OWC showed a positive effect on the loading on the main front wall. However, walls were modelled as beams, not capturing the structural behaviour properly. More research was dedicated to just the forcing on an OWC. Consecutive research (Ashlin et al., 2015; Ashlin et al., 2017) showed that the net horizontal force on the structure is about three times as large as the vertical force. Increasing wave steepness leads to larger pressures on the front wall, while the pressure in the chamber reduces. For low frequency waves, Goda's formula (Goda, 1974) overestimates the pressures on the front wall due to large energy absorption by the OWC. Kuo et al. (2015) found a positive effect on the pressures on a OWC breakwater, as they are lower than that on a regular vertical wall breakwater. Goda's approximation for wave pressures still showed reasonable results for estimating the wave forces, but underestimates the momentum, leaving the structure prone to overturning. The presence of an OWC in a breakwater enhances the global stability of the structure as was found by Boccotti (2007b). Overall it was concluded by Vicinanza et al. (2019) that the presence of an OWC in a vertical wall breakwater enlarges the stability of the structure. More research towards the impact of geometrical changes on the performance of an U-OWC was done by Ning et al. (2020). Especially an increased duct height showed an increased performance, which was to a lesser extent also the case for a larger duct width.

The lack of research on the actual structural response to wave loading leaves it as an unexplored field. With structural optimisation as a potentially viable method for cost reduction, this must change. This research aims to bridge this gap using combined 3D computational fluid dynamics (CFD) and structural finite element analysis FEM). By taking into account both the loading of the water waves and the response of the structure, a more complete view of the topic is obtained. The structural optimisation is aimed toward a more efficient design, with a lower material usage. As also stated

by Bruce and O'Callaghan (2013), there is a difference in optimal structural and functional design. A better understanding may bring these closer together. Through the applied methods, more insight is obtained on the structural behaviour as well, allowing for more efficient design methods in the future.

The remainder of the paper is split into four parts. Section 2 introduces the adopted numerical methods and the investigated case study. Results of the analyses are dissected in section 3. Section 4 contains the initial works of a new design method, which is derived from the earlier obtained results. Finally, a conclusion is drawn in section 5.

2   Methods

The research is carried out via the commercial numerical code Simcenter STAR-CCM+ v14.04.011-R8. It enables the user to have both fluid and solid domain within a single simulation. One-way or two-way coupling enables to directly investigate fluid-structure interaction. The research is based on the U-OWC device in Civitavecchia, Italy. This is the first realisation of an U-OWC, yielding an additional front wall. The wall has a positive influence on the eigenperiod of the device, which now lies closer to that of the incident waves, enhancing the sought resonance effect (Boccotti, 2007a). The device was built as part of a port enlargement project and contains 124 separate OWC chambers. A simplified cross section of the Civitavecchia device is depicted in Figure 1, containing the main dimensions (Arena et al., 2013). The transverse (out-of-plane) width of a typical chamber is 3.87 m. The structure is modelled as a single monolithic body. In reality, the back part is constructed as a caisson, with initially empty voids, which are later filled by either concrete or dredging material as ballast (Arena et al., 2013). This distinction is not made within the model, where everything is assumed concrete. Main interests of this study are the three transverse walls, here named the U-wall, front wall and back wall as labelled in Figure 1. Their initial

Figure 1: Adopted cross section of the REWEC3 caissons built in Civitavecchia, dimensions taken from (Arena et al., 2013)

thicknesses are 400 mm, 500 mm and 600 mm respectively. The figure also shows the adopted coordinate system. The aim of the structural optimisation is finding new minimum required thicknesses for each wall, based on loading by the incident waves.
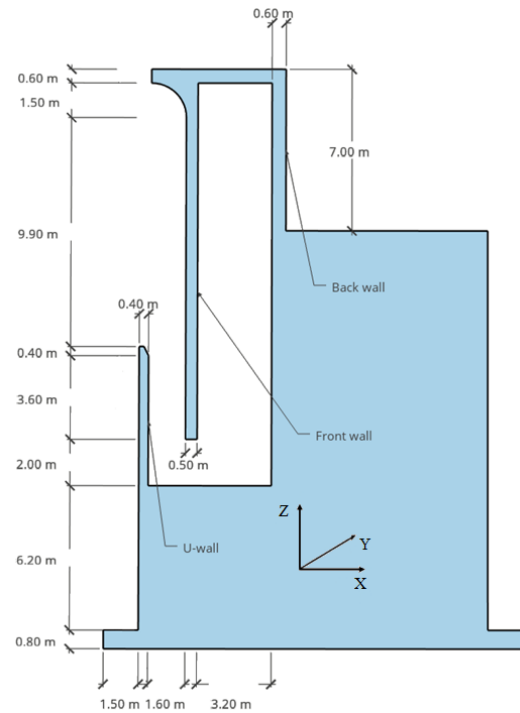
2.1 Methodology

The path to defining the structural optimisation consists of several steps, where the numerical model is only the first. In short: regular waves generated at the inlet boundary, propagate towards the device. Due to the one-way coupling applied in the simulation, the wave induced pressures are directly mapped on to the structural elements as external loads. From these loads, the stresses are found in the walls. The software does not allow for sectional forces such as normal forces and bending moments to be calculated directly. The stresses are therefore extracted and processed separately. First they are converted to normal forces and bending moments, upon which a new minimum required thickness is found. This is further elaborated on in Section 2.4. With this thickness, an optimisation potential is found, defined as the material that could have been used less to construct the walls according to the newly adopted method. In addition, the simulation is run again under operational conditions to quantify the energetic performance of the device. Both variants of the simulation are carried out as well for a set of geometrical changes to investigate how these influence the results. Potentially, a better design is found this way. The results found from the simulations under design conditions are also used to analyse the structural behaviour.

2.2 Model set-up

The numerical model contains three separate, but coupled, domains. These are the fluid domain, solid domain and turbine domain. The final model is at full scale and in 3D, containing one half of an OWC chamber. By making use of symmetry conditions at half the transverse width, the correct structural behaviour is simulated. Separate models were set up for the design and operational conditions, with the only differentiating elements being wave parameters used and total model length, which is adjusted for the different wave lengths.

2.2.1   Fluid domain

The fluid domain is a numerical wave tank in which waves propagate towards the OWC. It has been set up appropriately to be able to accommodate surface gravity waves (SIEMENS, 2019), with the accompanying settings elaborated on below. The flow in the tank is solved by the RANS-equations, where the Realizeable k-ε all y+ two layer turbulence model available in STAR-CCM+ is adopted. The Eulerian multiphase model is adopted to have both air and water within the same domain. Both fluids were modelled as incompressible. The interface between the different phases is tracked according to the Volume of Fluid (VoF) method.

An overview of the model boundaries is presented in Table 1 and Figure 2.

Table 1: Overview of boundary conditions.

| Boundary	Type	Description
Inlet	Velocity inlet	Generates the fifth order Stokes wave based on velocity profile of the wave.
Top	Velocity inlet	Aids the inlet boundary in generating the waves.
Outlet	Pressure outlet	Ensures the water level beyond the OWC remains still at all times.
Bottom	No-slip wall	Boundary of the numerical tank, imposes a zero flow velocity parallel to the wall.
Sides	Symmetry planes	Boundaries simulate symmetrical behaviour on both sides of planes. For fluids, this implies zero velocity perpendicular to the plane. For solids, this implies zero displacement perpendicular to the plane.
OWC geometry	No-slip wall	Interface between wave thank and structure, imposes a zero flow velocity parallel to the wall.
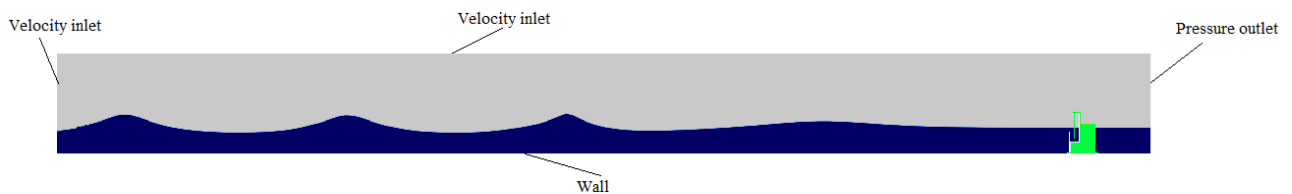
Figure 2: Overview of model boundaries.

A forcing zone was applied with a length equal to two times the wave length at the inlet boundary. Within this zone, the solving method for wave propagation gradually shifts from fully theoretical at the inlet to fully numerical at the end of the zone. It also acts as a relaxation zone and prevents reflection at the inlet boundary. (SIEMENS, 2019)

An overview of the model and wave parameters are presented in Table 2. Waves are generated at the inlet boundary according to fifth order Stokes theory as described by Fenton (1985). The wave characteristics to account for the design conditions are derived from suggested storm wave spectra of Civitavecchia (Arena et al., 2013) and adjusted through Goda's method for the definition of the design wave, ($H_{1/250}$) (Goda, 2000). The spectral significant wave height was multiplied by a factor equal to 1.8, while the peak period was multiplied with a factor 0.95 in order to account for the significant period. The wave in operational conditions has characteristics which are relatively close to optimal energetic circumstances (Arena et al., 2017). The wave tank in front of the OWC has a length of approximately four times the wave length. The width is equal to half the transverse chamber width.

Table 2: Model and wave parameters for operational and design conditions.

Condition	Model parameters			Wave parameters			
	Length [m]	Width [m]	Height [m]	Water depth [m]	Wave height [m]	Wave period [s]	Wave length [m]
Operational	650	1.935	60	15	2.5	6.3	58.5
Design	300	1.935	60	15.5	10.8	9.9	132.8

The mesh is generated using the surface remesher (optimises surface for volume meshing) and trimmer (generates volume mesh) models (SIEMENS, 2019), creating hexahedral cells. The mesh resolution in the wave zone is based on best practice for wave modelling and is derived from the wave parameters (Perić, 2017): A wave should not propagate more than 50% through a single cell, to prevent damping of the amplitude. An aspect ratio of length:height of 2:1 was adopted. Out of several tests of mesh sizes, the ones presented in Table 3 led to the best results.

Table 3: Mesh sizes in wave zone.

Condition	Wave zone [m from bottom]	Cell length [m]	Cell height [m]
Operational	8 to 26	0.3	0.15
Design	13 to 19	0.6	0.3

Further local refinement is applied in the vicinity of the OWC. A detailed specification is presented in Table 4. The different meshing zones are displayed in Figure 3. The cells in the Y-direction (perpendicular to plane) are kept larger, allowed by the predominant 2D flow, to not have an unnecessary high number of cells. A prism layer mesh was added along all wet wall boundaries coinciding with the structure to properly capture the boundary layer. It has a thickness of 0.1 m, split in seven layers with a stretching ratio of 1.5. With this, the values for y+ remain below 200 during the simulations. The selected two-layer turbulence model accounts for the correct solving method of near-wall flow, dependent on the transient y+ values (SIEMENS, 2019). The fluid mesh consists of roughly 2.5 million cells, which accounts for more than 90% of the total number of cells in the simulation. Of these, again 90% is located in and around the OWC.
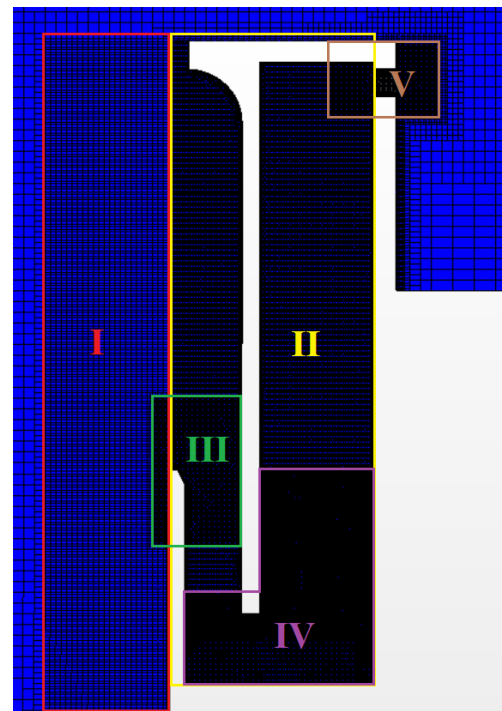

Figure 3: Used meshing zones in and around the OWC.

Table 4: Mesh sizes in and around the OWC.

Zone	dx [mm]	dy [mm]	dz [mm]
I	150	300	75
II	75	300	37.5
III	37.5	75	37.5
IV	18.75	150	18.75
V	37.5	37.5	37.5

2.2.2 Solid domain

The solid domain contains the entire breakwater structure as already depicted in Figure 1. It is modelled as an isotropic, linear elastic, solid body. A semi-circle is cut out at the location of the turbine with a diameter of 0.75 m. The Civitavecchia device is made out of concrete with class C35/45 (Arena et al., 2013). The material properties are set appropriately, yielding a density of 2500 kg/m^3, a Poisson's ratio of 0.2 and a Young's modulus of 15 GPa. The fluid structure coupling model also is enabled in the solid domain.

All boundaries, except for one, are wall boundaries. Only the actual symmetry plane of the structure, i.e. halfway the transverse width, is set to the symmetry boundary type, implying zero deformation normal to this plane. The structure is constrained at the bottom and other side boundary. The bottom constraint resembles the frictional forces keeping the

breakwater in place in reality. This prevents rigid body motion and governs the stability of the structure. The side constraint resembles the rigid connection to the longitudinal walls separating neighbouring chambers. It ensures the model captures the correct structural behaviour. Furthermore, a static load of 5 kN was added at the orifice, representing (half) the dead weight of the turbine.

The mesh for the structural domain is created with the surface remesher and tetrahedral mesher models. A base size of 1 m used to fill up the solid part of the structure. The output here is of no significance, rendering refinement useless. The mesh inside the walls is refined to have four cells over the wall thickness. The structural mesh contains roughly 180,000 cells. Mid-vertex nodes are activated while running the simulation, creating quadratic elements.

2.2.3   Turbine domain

The turbine domain is located at the location of the real turbine. It is represented by a porous region, as similarly done in Scarpetta et al. (2017). The region induces a pressure loss Δp, resembling the damping otherwise induced by the turbine, following the relation given by the equation,

$$\frac{\Delta p}{L} = -(P_i|v| + P_v)v \tag{1}$$

dependent on the flow velocity v through the turbine. It is created by setting the fluid continua to a porous region type. The damping effect is controlled by inertial and viscous damping coefficients P_i and P_v. The porous inertial resistance is set to 70 kg/m^4 and the porous viscous resistance is set to 5600 kg/m^{3}s. The values are based on the resistance coefficients (R_i and R_v) presented by Scarpetta et al. (2017) for the Civitavecchia design and information on the turbine in Civitavecchia. The resistance coefficients were multiplied with the ratio of turbine lengths adopted in the different models to adjust for the differences in modelled turbine length L. The damping coefficients are defined by,

$$P_i = 0.5\rho_a R_i \quad \text{and} \quad P_v = \mu_a R_v \tag{2}$$

where ρ_a is the air density and μ_a is the dynamic viscosity of air. The turbine used in Civitavecchia is a Wells turbine, which has a linear relationship between flow velocity and pressure drop (Falcão and Henriques, 2016). By assessing the pressure drop in the porous region once the simulation was completed, it was confirmed this behaviour was captured quite well. In the simulation under design conditions, all damping values are halved by assumption to qualitatively include the effect of emergency pressure valves opening up in reality during storms. The valves relieve the chamber of excess pressures, allowing a larger rise of the water column, while reducing the excitation on the rotor blades. Halving the values proved to have a similar (qualitative) effect. In passing, it is worth mentioning that the same concept was employed recently in operational conditions by utilizing relief valves working in parallel to PTOs. Indeed, Scialò et al. (2021) showed that such an implementation is useful for limiting conveniently the turbine rotational speed (via air pressure reduction) with the purpose of ensuring that the PTOs are operating around the optimal working conditions.

The mesh in the porous region is created using the surface remesher and trimmer models. It consists out of roughly 3000 hexahedral cells with a size of approximately 40 mm.

2.2.4   Interfaces and coupling

The numerical model is one-way coupled, from fluid to structure. Interfaces are placed on all surfaces on which relevant pressures act. This maps the pressures directly onto the structure during every time step. The pressures are taken as external loads, which cause a certain stress state in the structure. One-way coupling is assumed to be sufficient, as deformations are expected to be very limited and will therefore not affect the flow. Due to the stout nature of the overall structure (i.e. recurved crownwall and rear side chamber), the coupling is set to a linear static analysis, implying that no structural inertia effects or load history are taken into account while calculating the stresses in the structure. Similar to the displacements, the dynamic aspects are not expected to largely affect the developed internal stress. It is highlighted that a similar crownwall has been recently investigated in Dermentzoglou et al. (2021), where the dynamic response was found to be relevant for the overall structural integrity under the Confined Crest Impact, (Castellino et al., 2021; Castellino et al., 2018). However, the crownwall investigated by (Dermentzoglou et al., 2021) was only supported by a slender concrete element, whereas in the proposed case the combined effect of the elements of the rear chamber produces a stiffer and more resilient structure.

Additional interfaces are placed at the front and back of the turbine domain. These are of the internal type, allowing continuous flow between the fluid domain and porous zone.

2.2.5 Time

Time is discretised in two stages, applying second order discretisation in both. Stage 1 starts with the start of the simulation and ends once the first wave reaches the device. A constant time step is applied here based on wave parameters and mesh density, following the equation (SIEMENS, 2019),

$$\Delta t = \frac{T}{2.4n} \tag{3}$$

where T is the specified wave period and n is the number of cells in one wavelength. The fixed time steps during stage 1 are 0.02 s and 0.013 s for the simulations under design and operational conditions respectively.

Once the first wave reaches the OWC, stage 2 commences, during which the time step is determined within the simulation by the adaptive time step model. It determines the time step based on the Courant number and is free to vary between fixed boundaries, with a minimum value of 0.002 s, while the maximum time step is set equal to the fixed value of stage 1. The Courant number settings apply to the full modelled domain and are set to a target mean value of 0.4 and a target maximum value of 15. The latter is set to cancel out the effect of very large Courant values in the prism mesh around sharp corners.

2.2.6 Validation

In order to have confidence in the numerical results, the fluid domain of the model is validated first. Wave pressure is the main load on the walls. Having the right magnitude of wave pressures therefore is of great importance. The validation is done based on earlier done experiments, carried out on scale models of several OWC geometries with several wave parameter sets (Rivero, 2018). The validation here is limited to four out of six configurations for one wave of height $H = 0.05$ m and period $T = 2.3$ s. The water depth is 0.47 m. The OWC geometry was shaped with wall boundaries inside of the fluid domain. Results of the validation are shown in Figure 4, where the surface elevation inside the chamber is compared for two geometries.
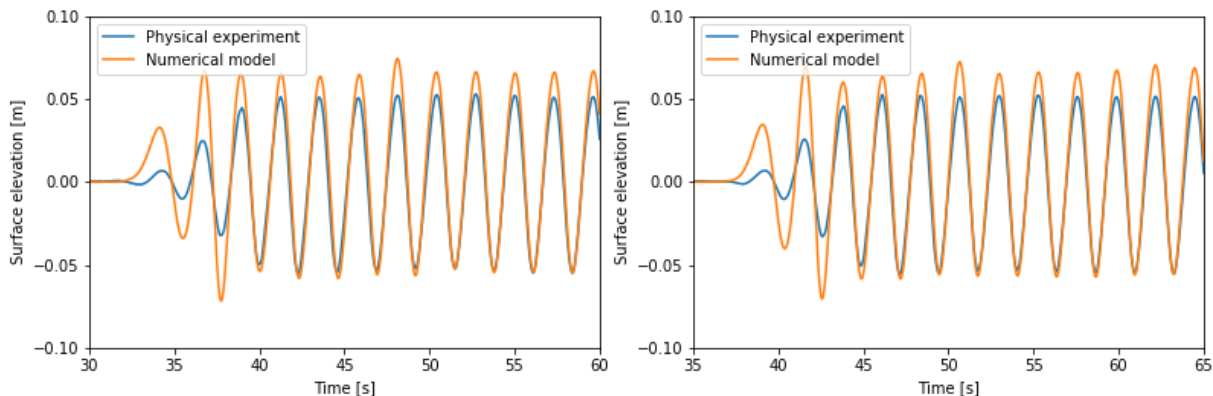

Figure 4: Comparison of surface elevations in a conventional OWC chamber, measured during experiments and found from numerical modelling for a fully open OWC chamber (left) and a closed chamber (right).

A consistent discrepancy in observed oscillation amplitude was found between the numerical and physical experiments results. The magnitude is overestimated by the numerical simulation in all cases, by an average of 15%. The difference is only present at the peaks, as all troughs do line up. The periodic behaviour is captured quite well.

Further validation was done to verify whether wave pressures were captured correctly or not. Pressures were measured for a wave interacting with a vertical wall and compared to the solution presented by Goda (1974), as shown in the left panel of Figure 5. Both solutions follow the same pattern in pressure distribution, with the peak value at the still water level. The peak value is slightly larger in the simulations than found from Goda's schematisation. Additionally, the fluid-structure interaction was tested by assessing the hydrostatic pressure on a vertical wall and comparing these with the exact analytical solution. From both methods, vertical stresses along the wall height were found, as can be seen in the right

panel of Figure 5. It is a near perfect match, where the error at the constraint is explained by singularities, regularly occurring in such locations in numerical structural analyses.
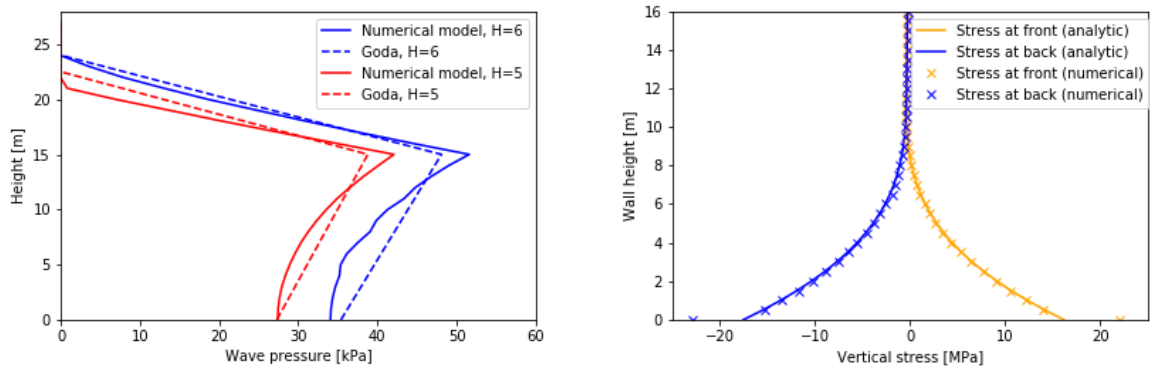

Figure 5: Validation of wave pressures found in the numerical model (left) and the fluid-structure coupling (right).

In an attempt to increase the confidence in the model, additional validation tests were carried out and compared with the experimental data. These include using waves of different periods, other turbulence models and different combinations of mesh size and time step. In all cases, a similar discrepancy was observed, hence we believe that the discrepancy between the numerical and physical modelling is mainly due to the inaccuracy of the laboratory results rather than the numerical model. This believe is strengthened by the results from Figure 5.

2.3 Geometrical changes

A set of geometrical changes was applied to the original Civitavecchia geometry. The idea is to investigate how certain changes influence the results. This holds for structural optimisation, but especially for structural behaviour. By testing a different geometry under both design and operational conditions, a conclusion can be drawn whether this is a viable alternative design or not. A profit due to structural optimisation may be cancelled out by a loss in energetic performance.

An overview of all geometrical changes tested is shown in Table 5. What these dimensions are in the geometry is shown in Figure 2. The original U-wall height is 13 m, measured from the bottom of the structure. The original duct width is 1.6 m. The corners originally have 90° angles. The changes for U-wall height and duct width were inspired by earlier research (Ning et al., 2020) and were found to lead to an increase of energetic performance. Applying rounded corners was done based on results presented in Scarpetta et al. (2017), where flow was shown to be re-circulating in these bottom corners. A rounded corner potentially leads to a more directed flow and weaker local dissipations. Together with the simulation of the current Civitavecchia geometry, from now on denoted as 'CUR', this gives eight geometries that will be tested under two circumstances, totalling sixteen simulations.

The last column of Table 5 shows the change in material usage only due to the geometrical change. This is going to play a critical role while defining the final optimisation potential and must be included for a fair comparison.
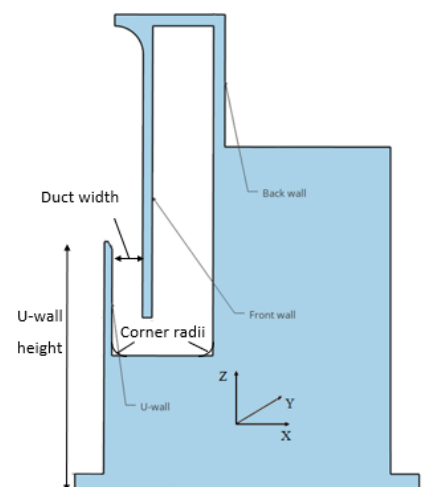

Figure 6: Changing dimensions of the OWC geometry.

Table 5: Set of geometrical variations of the reference geometry CUR.

Name	Changing dimension	New dimension [m]	Change in material usage [m3/m]
H125	U-wall height	12.5	-0.2
H135	U-wall height	13.5	+0.2
H140	U-wall height	14.0	+0.4
W12	Duct width	1.2	-2.8
W20	Duct width	2.0	+2.8
W30	Duct width	3.0	+9.8
R10	Corner radius	1.0	+0.43

2.4 Processing and finding the new thickness

The results of the numerical simulation are only stress values in the structure. Normal and shear stresses are measured in both in-plane wall directions along the wall height on both sides and at two locations, being at the constraint and at midspan. This is also shown in Figure 8. The stresses are measured with a height interval of 0.5 m. Per wall and per measuring location, the data is converted to plots showcasing, per time step, the stress at both sides of the wall simultaneously. Combining all plots gives the full transient stress distribution.

Based on the linear elastic behaviour of the material and applying classical mechanics concepts, the normal stresses are decomposed in the individual contributions due to a normal force and a bending moment. Multiplying these with cross sectional area and section modulus respectively gives the actual normal force and bending moment in the cross section.

From each set of normal force and bending moment, a new thickness is calculated. The largest value found for each wall is the new minimum required thickness. Three equations, based on Eurocode 1992-1-1 are used for this, one for a compressive normal force (Eq 4), one for a tensile normal force (Eq 5) and one for the shear criterion (Eq 6). That is,

$$M_{Ed} = N_c(0.5h - \beta x_u) + \rho_s hbf_{yd}(0.5h - a) \quad \text{with} \quad x_u = \frac{N_{Ed}}{\alpha bf_{cd}} \tag{4}$$

$$0.5\rho_s hbf_{yd} = 0.5N_{Ed} + \frac{M_{Ed}}{h - 2a} \tag{5}$$

$$v_{Rd,c} = 0.035k^{3/2}f_{ck}^{1/2} \quad \text{with} \quad k = 1 + \sqrt{\frac{200}{d}} \leq 2.0 \tag{6}$$

where, M_{Ed} is the bending moment in the wall, N_{Ed} is the normal force in the wall and N_c is the normal force in the concrete. From horizontal equilibrium, it follows $N_c = N_{Ed}$ in the case of a compressive normal force. h is the wall thickness and b is the width of the evaluated section, here $b = 1000$ mm. a is the distance from the edge of the section to the center of the reinforcement, assumed at 80 mm. f_{yd} is the reinforcement tensile stress, assumed at 200 MPa. ρ_s is the reinforcement ratio, assumed at 1%. f_{ck} and f_{cd} are the characteristic and design concrete compressive strengths respectively. The Civitavecchia breakwater was constructed using concrete class C35/45 (Arena et al., 2013), which was also applied here. The values of f_{ck} and f_{cd} are derived from this, where $f_{ck} = 35$ N/mm^2 and $f_{cd} = 23,3$ N/mm^2, including a material factor of 1.5. x_u is the height of the concrete compressive zone and α and β are shape factors respectively valued at 0.75 and 0.39, d is referred to as the useful section height, defined as $h - a$.

Two main assumptions were made, allowing easier calculations. By reducing the reinforcement tensile stress to 200 MPa, the SLS criterion for a maximum crack width of 0.3 mm (exposure class XS3 (Arena et al., 2013)) according to Eurocode 1992-1-1 is accounted for. The reinforcement ratio is fixed at 1%, an empirical optimum, which gives the equations a closed solution for the wall thickness.

3   Results

The results are divided into two parts. The structural optimisation is described first, followed by the structural behaviour.

3.1   Structural optimisation

The structural optimisation is quantified by the optimisation potential. It is defined as the reduction in the amount of material required to construct the OWC, expressed as a percentage. A positive value means a reduction in material usage. The reduction in material usage follows from the newly found minimum required thicknesses per wall, which are the result of the new design method adopting the coupled numerical model. The difference is determined for each wall first which, once combined, gives the optimisation potential for the full structure.

The optimisation potential is compared to the change in energetic performance per geometry. The optimal structural design is by definition not equal to the optimal geometrical design, as they have different goals. The optimal geometrical design yields the largest energy production, based on which its dimensions are determined. The optimal structural design aims to have the lowest material usage while still maintaining structural integrity. To account for both design goals, both results for optimisation potential and energy production are taken into account in determining whether a certain geometrical change is a viable alternative to the Civitavecchia geometry. The energetic performance is measured in terms of average oscillation amplitude in the chamber under operational conditions.

3.1.1   Benchmark case

First, a base case analysis is performed for the current Civitavecchia geometry, as shown in Figure 1. The simulation under design conditions leads to a new thickness for each wall. These results act as a benchmark, CUR (the current geometry), that will act as reference value for the results of the tests on the geometrical changes. Table 6 contains the results, showing the reduction per wall. The reduction per wall is multiplied by the respective wall height to find the absolute volume of concrete. This leads to an optimisation potential of 35% overall, or approximately 4.6 m^3/m per running meter of device.

Table 6: Result of the benchmark test, the actual Civitavecchia geometry, denoted as CUR.

Wall	Original thickness [mm]	New thickness [mm]	Difference [%]	Difference [m^3/m]
Front	500	321	36	2.5
U	400	280	30	0.7
Back	600	362	39	1.4

3.1.2   Results from geometrical changes

Each geometrical change is tested one by one. First the geometry of the structure is changed in both versions of the model, after which the simulations are run. The results are gathered per geometry and then expressed relatively to the results from CUR. This is done to isolate the contribution from the geometrical changes, which is of main interest here.

The results for all geometries are presented in Figure 7. The horizontal axis shows the relative energetic performance. The vertical axis shows the relative optimisation potential, where a positive value indicates towards further reduction in material usage. CUR is positioned at the origin. CUR performs best in terms of energy production. Looking at optimisation potential, only W12 shows a significant positive optimisation potential relative to CUR. W20 and W30 show a large increase in material usage, while the remaining geometries show a similar optimisation potential as CUR. Evaluating the results more in depth leads to the conclusion that the values for the optimisation potential are governed by the current geometrical change. In other words, by performing the geometrical change, the material usage also changes by the amounts stated in

.

For the case of W12, narrowing the duct means also narrowing the solid mass of concrete underneath it, while widening the duct, widens the solid mass. This explains why W20 and W30 show such a large negative potential. Apparently, the geometrical changes do not have a significant effect on the loading on the walls as will also be seen in Section 3.2, hence they have approximately the same thickness for each geometry.
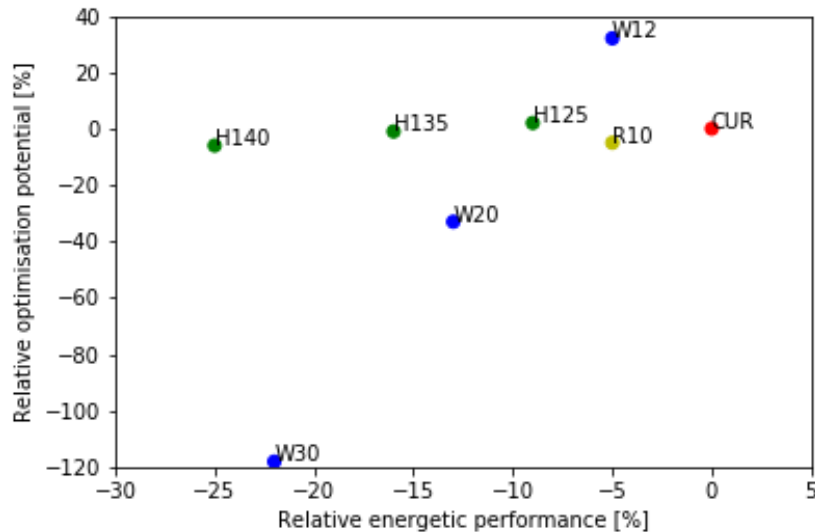

Figure 7: Results for all tested geometries, expressed relative to CUR. Relative energetic performance measured as average oscillation amplitude in the chamber. Relative optimisation potential defined as additional optimisation relative to CUR. Numbers denote the respective dimension: H for front wall height measured from bottom (13 m for CUR), W for front duct width (1,6 m for CUR) and R for corner radios (0 m for CUR).

The results for energetic performance are in contradiction with results found by Ning et al. (2020) for similar geometrical changes. A closer look reveals different ranges of relative parameters were used between these researches. The parameters are the ratios of wall height to water depth and wave number to water depth. Ning et al. (2020) stated that having a U-wall reaching closer to the still water level increases the energy production. Apparently, H135 and H140 are too close to the water surface, distorting the inflow of water, where CUR seems to be right on the limit, as H125 also performs worse. The loss in performance for wider ducts is likely to be caused by a larger recirculation of flow inside the duct once it becomes wider. A wider duct would reduce the forced singular directionality of the flow. In this regard, numerical results are shown in the following sub-section, where it is shown that, during inflow, the flow is directed downwards in the back of the duct, but simultaneously upwards in the front of the duct. A more circular flow inside of the duct implies less inflow of water to the main chamber and thus a lower amplification.

Based on the results in Figure 7, only W12 can be appointed as a potential viable alternative geometry. It does have a lower energetic performance than CUR, but also a significantly larger optimisation potential. To confirm this statement, a further economic analysis is required, monetising both the loss in energetic performance and saving in material usage.

3.2 Structural behaviour

The analysis of structural behaviour is based on the results from the simulations under design conditions. These represent the circumstances that lead to the extreme forces the structure has to endure. An analysis of these forces is carried out in this section. The goal is to obtain a better understanding of the structural behaviour of the OWC and what role the forces play in this. This is done in two steps. First, for each wall per geometry, the governing load combination is found. This combination is defined as the pair of normal force and bending moment that leads to the largest thickness. Then, for each combination, two additional properties are found. These are the location in the wall and the moment in time this combination occurs at, so that it should be known for future designs where and when the critical forces in each wall are expected.

3.2.1 Load combination

In total, three thicknesses are calculated from each measurement point in the simulation. In these points, normal stresses are measured in two directions: the Y-direction, which is the transverse horizontal direction and the Z-direction, which is the vertical direction, see Figure 1. Additionally, the shear stresses are measured. This gives the three load cases used in the analysis. Each load case results in its own thickness, found by solving the equations stated in Section 2.4.

The results are presented per wall, in Table 7 for the front wall, Table 8 for the U-wall and Table 9 for the back wall. For each load case, the thickness is reported. For the in-plane directions, also the force magnitudes are presented.

Table 7: Governing load combinations per geometry for the front wall. A bending moment is defined positive if it generates a compressive stress at the frontside of the wall. The largest thickness per geometry is printed in bold. The load case that caused this thickness therefore is the governing load case. If a maximum value was found at midspan, an asterisk is added.

| Config. | In Y-direction | | | In Z-direction | | | Shear |
	Bending moment [kNm]	Normal force [kN]	New thickness [mm]	Bending moment [kNm]	Normal force [kN]	New thickness [mm]	New thickness [mm]
CUR	-32	26	**280**	-15	-92	194*	**280**
H125	-31	30	275	-14	-86	192*	**280**
H135	-32	32	**280**	15	115	242*	280
H140	-30	23	275	17	133	252*	**280**
W12	-32	52	**284**	-12	-42	200*	280
W20	-32	-13	269	-16	-111	191*	**280**
W30	-34	49	**288**	18	133	254*	280
R10	-30	36	275	-6	5	191	**280**

Several observations are done based on the values in Table 7. When looking at the values per column, they show a strong consistency in magnitude. Only W30 deviates from this. The Y-direction seems to yield the largest loads, with a bending moment of around 50 kNm. The forces in the Z-direction are considerably lower, making the Y-direction overall governing. An average required thickness of 325 mm was found for the front wall. The shear criterion for all geometries leads to a required thickness of 280 mm. This actually is the minimum value that can be obtained by Eq 6 with the adopted parameters. The shear stresses found during the simulation are low, so this minimum thickness is sufficient.

Table 8: Governing load combinations per geometry for the U-wall. A bending moment is defined positive if it generates a compressive stress at the frontside of the wall. The largest thickness per geometry is printed in bold. The load case that caused this thickness therefore is the governing load case. If a maximum value was found at midspan, an asterisk is added.

| Config. | In Y-direction | | | In Z-direction | | | Shear |
	Bending moment [kNm]	Normal force [kN]	New thickness [mm]	Bending moment [kNm]	Normal force [kN]	New thickness [mm]	New thickness [mm]
CUR	-51	9	**321**	-10	2	210	280
H125	-53	1	**323**	-11	-1	211	280
H135	-49	16	**319**	-10	2	208	280
H140	-57	10	**333**	-11	2	214	280
W12	-56	7	**330**	-10	1	213	280
W20	-50	6	**318**	-10	0	209	280
W30	-44	81	**318**	-10	13	210	280
R10	-53	4	**324**	-11	2	211	280

The U-wall shows more complex behaviour, as can be seen from Table 8. There is still a consistency in the majority of the values along the table columns, but the governing load case now varies between the Y-direction and shear. The shear criterion is however governing with the minimum value of 280 mm following Eq 6. As the values found for the Y-direction are very close, these will still be used during further analysis. The Z-direction shows deviating results, with very large normal forces. These were found to be singularities, i.e. common numerical artefacts occurring near sharp corners in the numerical model causing very local peak values in stresses. These values were filtered out and replaced by the thickness found at the largest bending moment.

Occasionally, this value still coincides with the absolute largest thickness found, still leaving inconsistencies. Especially a large tensile force leads to a large thickness, while an increasing compressive force only has a positive effect on the cross section capacity. Contrary to earlier results, the governing combinations were found at midspan, instead of near the constraint. Still, in all cases the thickness found in Z-direction is lower than that in Y-direction. The Y-direction therefore is still seen as the governing load case. Bending moments have an average value of 32 kNm, resulting in a wall thickness of 278 mm.

Table 9: Governing load combinations per geometry for the back wall. A bending moment is defined positive if it generates a compressive stress at the frontside of the wall. The largest thickness per geometry is printed in bold. The load case that caused this thickness therefore is the governing load case. If a maximum value was found at midspan, an asterisk is added.

| Config. | In Y-direction | | | In Z-direction | | | Shear |
	Bending moment [kNm]	Normal force [kN]	New thickness [mm]	Bending moment [kNm]	Normal force [kN]	New thickness [mm]	New thickness [mm]
CUR	-68	51	**362**	-23	-100	217*	280
H125	-68	28	**359**	-24	-107	217*	280
H135	-67	50	**359**	-23	-99	216*	280
H140	-70	53	**366**	-24	-106	218*	280
W12	-67	25	**356**	-23	-104	216*	280
W20	-69	26	**359**	-23	-106	217*	280
W30	-69	52	**364**	-24	-103	217*	280
R10	-65	23	**351**	-22	-111	211*	280

The back wall showed very similar behaviour to that of the U-wall. The values are presented in Table 9. There again is a strong consistency along the values in the table columns. The Y-direction also clearly forms the governing load case again with a bending moment of 68 kNm and a thickness of 359 mm. In the Z-direction, singularity values occurred just like they did in the U-wall. The thicknesses reported in this direction all are from the location of the largest (absolute) bending moment. This now leads to similar values for each geometry, just as in all other columns of the table. The values in Z-direction were also found at midspan again.

Overall, several main interesting conclusions can be drawn from the analysis. The governing load direction always is the Y-direction. The corresponding loads are always found in the constraint. Additionally, the maximum thickness found was, for almost all cases, the same as found at the location of the maximum bending moment. This implies that the thickness is mainly determined by the bending moment and not so much by the normal force. The bending moments per wall showed strong consistency in magnitude among the different geometries. This indicates the limited influence the geometrical changes have on the loading, which was already observed in the analysis on the optimisation potential. Shear stresses in the walls are limited, leading in all cases to the minimum required thickness defined by Eq 6.

For the remainder of the analysis, only the load cases of normal force and bending moment in Y and Z-direction are considered.

3.2.2 Governing sections along the walls

For each calculated thickness, the corresponding measurement point can be found by tracing back through the data. This is done here for the largest identified thicknesses. By doing this per wall for each load case and geometry, potentially a trend is found in where these occur. It would then be known what is the critical cross section of each wall and where it can be expected. The results are gathered in Table 10. Heights are measured from the bottom of each wall. Relative heights are shown in Figure 8.

Again, the values per table column are consistent. W30, with a duct width of 3,0 m, again is observed as the geometry that deviates most from the others. The front wall shows the same position for both directions, somewhere in the upper half of the wall. The U-wall and back wall again show similar behaviour. In the Y-direction, the position of the governing loads is around half the height. In the Z-direction, this is at the constraint, which is explained by the cantilever effect.
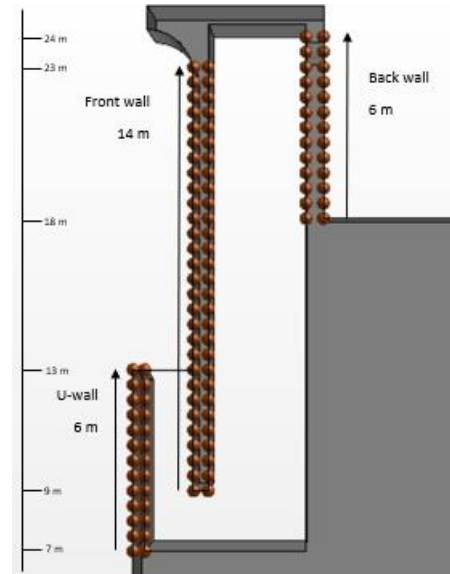

Figure 8: Relative heights of the three main walls in the OWC structure.

Table 10: Heights in the walls were governing load combinations occurred. Measured from the bottom of the respective wall. If a maximum value was found at midspan, an asterisk is added.

Config.	In Y-direction			In Z-direction		
	Front wall [m]	U-wall [m]	Back wall [m]	Front wall [m]	U-wall [m]	Back wall [m]
CUR	10.5	2.0	3.0	10.5	0*	0*
H125	10.5	2.5	3.0	10.0	0*	0*
H135	11.0	2.5	3.0	10.5	0*	0*
H140	10.5	2.5	3.0	10.5	0*	0*
W12	11.0	2.5	3.0	10.5	0*	0*
W20	10.5	2.5	3.0	10.5	0*	0*
W30	7.0	3.0	3.0	6.5	0*	0*
R10	11.0	3.5	2.5	10.5	3.5	0*

3.2.3 Timing

Finally, the moment of occurrence is found from the dataset. Similar to tracing back at which measurement point certain stresses were found, it is also possible to find at which time instant these stresses occurred. These can then be converted to the in-simulation time. All design simulations were run with the same time signature, waves and model length, meaning waves reach the device at the same moment of the respective simulations. That also means oscillation cycles are in sync with each other and the time of occurrence between different simulations may be compared. The results are presented in Table 11 where the simulation time is given for the governing load combinations in both directions. At the start of the simulation, $t = 0$ s, the first wave is generated at the inlet. At approximately $t = 40$ s, the head wave reaches the OWC. At $t = 80$ s, the simulations were ended.

Table 11: Moments of occurrence of the governing load combinations per geometry.

Config.	In Y-direction			In Z-direction		
	Front wall [s]	U-wall [s]	Back wall [s]	Front wall [s]	U-wall [s]	Back wall [s]
CUR	65.4	68.2	47.3	65.4	68.2	47.3
H125	65.3	68.5	47.3	65.4	68.5	47.3
H135	65.0	68.2	47.3	65.0	65.3	47.3
H140	65.1	68.4	47.3	65.1	61.6	47.3
W12	65.1	68.6	47.3	65.1	68.6	47.3
W20	65.5	68.6	47.3	65.1	68.6	47.3
W30	69.2	68.7	47.4	69.2	61.5	47.4
R10	65.6	68.4	47.4	65.6	68.4	47.4

It is now observed that the values in the columns of the same wall are very similar. This implies the moment of occurrence is independent of the load case. This only makes sense though, as the forces in Y and Z-direction are generated by the same external load. Peak values are therefore likely to occur simultaneously. Only the U-wall deviates slightly from this trend, which can be explained by the values for the Z-direction in Table 9. The singularities cause different cases to be governing across the different geometries, also causing two times of occurrences. The values for the front wall and U-wall lie quite close, meaning they occur during the same wave, while the governing values for the back wall occur during a different wave.

3.2.4   Combination of findings

Next, all findings above are combined per wall to give a single explanation of why this is the governing load scenario for that wall. Added information for this analysis is the surface elevation in the chamber and in front of the chamber, above the duct. An example of what this looks like is given in Figure 9. The figure shows the surface elevations in the OWC chamber and just in front of the chamber, indicated by the dashed lines. These visualise the cyclic hydrodynamic behaviour under the wave loading. The dashed orange line shows the different phases of the oscillation cycle of the water surface in the main chamber are observed. The peaks denote the moments of maximum and minimum water level in the chamber. A rising graphs indicates inflow of water, while a falling graphs corresponds to outflow of water out of the chamber. The vertical lines in the chart represent the time of occurrence of the governing load case for each wall, as reported in Table 11. Combining these with the surface elevation plots, allows the time of occurrence to be coupled to a specific phase in the oscillation cycle. Furthermore, the (water) pressures and displacements are checked to help explain the identified forces. A detailed analysis for each investigated structural component is presented below.
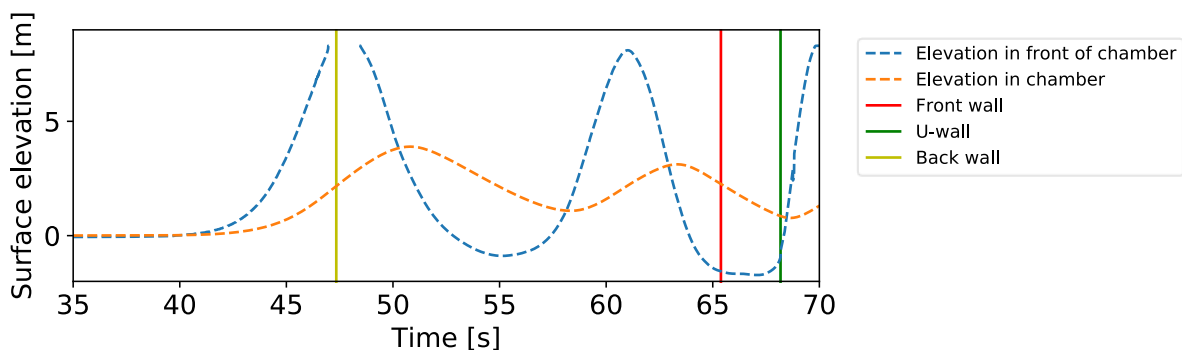

Figure 9: Measured surface elevation around the OWC and moments of occurrence of governing load combinations.

It must be mentioned that, due to the relatively deep water at the toe of the structure, the proposed analysis is based on non-breaking wave conditions. However, the risk of breaking waves is present for the design wave condition. Under such violent loading condition, the assumed static response of the structure would not be valid and a more comprehensive dynamic model would be required.

Front wall

The governing scenario for the front wall is depicted in plots in Figure 10. From Figure 9, it appears the scenario occurs while the rate of outflow of water from the main chamber is at its highest. This generates an underpressure above the water column, making the front wall bend inwards, as also observed in the left panel of Figure 10. This would create a positive bending moment at midspan of the front wall. As the walls are clamped on both sides, this results in a negative bending moment in the constraint. This is confirmed by values reported in Table 7 and the plot in the right panel of Figure 10. The position in the wall appears to be halfway the height of the volume of air that is above the water column at that moment, indeed, the left panel of Figure 10 shows the net pressure (pressures at both sides evened out) is at its largest here.
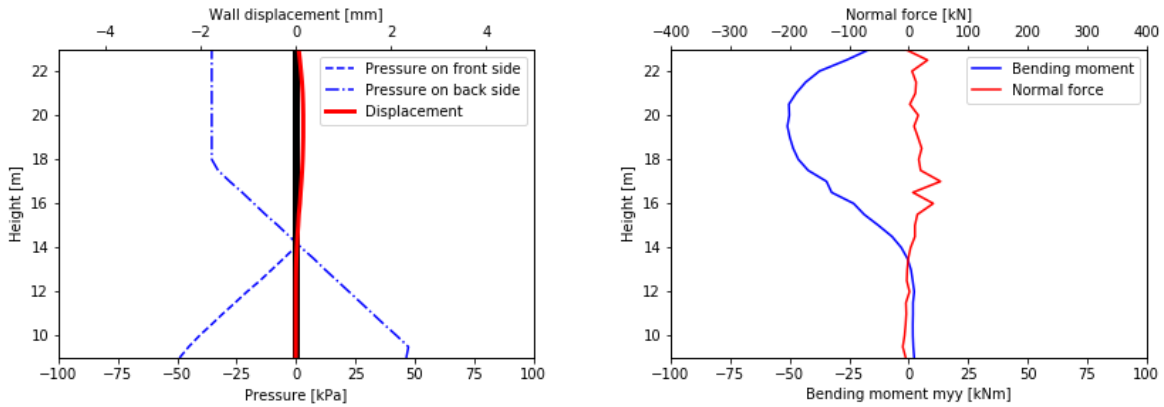

Figure 10: Pressure and displacement (left) and bending moment and normal force distribution (right) for the front wall at the moment of the governing load combination for the front wall. The pressure is shown on the side of the wall it acts on. The relevant OWC geometry is included in black.

U-wall

The governing scenario for the U-wall is depicted in plots in Figure 11. From Figure 9, it appears that the critical scenario occurs once a new wave approaches the OWC. The water level in the chamber is at its lowest at this point in the oscillation cycle of the water column. The approaching wave induces large pressures, likely due to the momentum on the frontside of the wall, pushing the wall towards the chamber. This is also observed in the left panel of Figure 11. This creates a positive bending moment at midspan in the Y-direction and therefore a negative bending moment at the constraint, which was also reported in Table 8. The governing forces occur just below half the height. This corresponds with the location of the largest deformation.
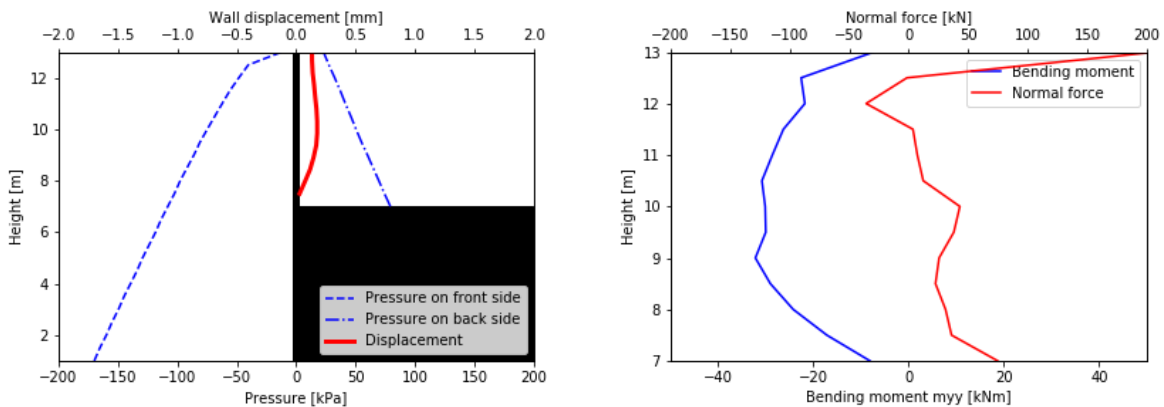

Figure 11: Pressure and displacement (left) and bending moment and normal force distribution (right) for the front wall at the moment of the governing load combination for the U-wall. The pressure is shown on the side of the wall it acts on. The relevant OWC geometry is included in black. Note that there is a difference in vertical axis range between both plots.

Back wall

The governing loading scenario for the back wall is depicted in Figure 12. From Figure 9, it appears the scenario occurs while the rate of inflow of water into the main chamber is at its highest. The largest inflow rate also causes the largest air pressure in the chamber. This overpressure makes the back wall bend outwards, as shown by the left panel of Figure 12. The pressures generate a positive bending moment at midspan in Y-direction and therefore a negative bending moment at the constraint, as also highlighted in Table 9. The governing loads occur halfway the height, which is the expected location for a wall constrained at two ends.
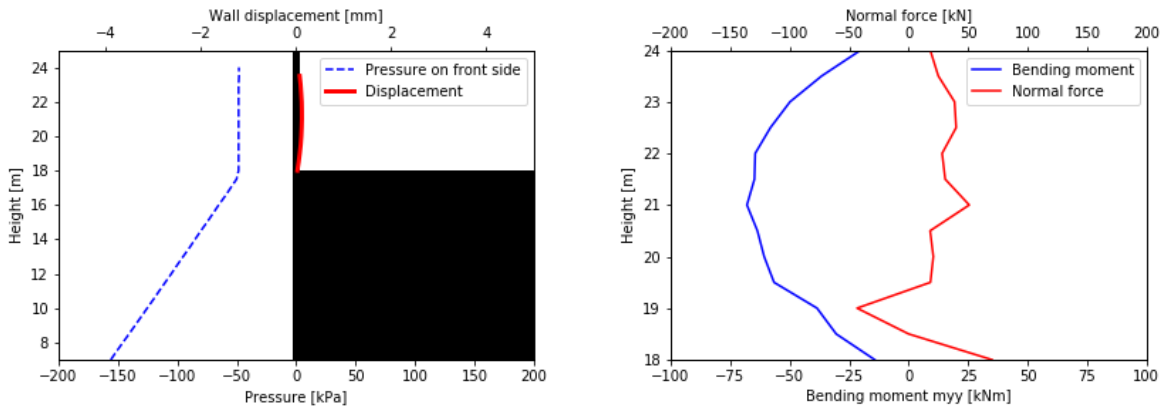

Figure 12: Pressure and displacement (left) and bending moment and normal force distribution (right) for the front wall at the moment of the governing load combination for the back wall. The pressure is shown on the side of the wall it acts on. The relevant OWC geometry is included in black. Note that there is a difference in vertical axis range between both plots. The red line is shortened due to the presence of the orifice.

3.2.5   Summary

A clear insight has been obtained on where and when critical forces may happen. It is also known in what direction these forces occur. Looking back at the magnitude of forces found, it seems the walls thickness is governed by the bending moment, as normal forces are limited. The bending moments in Y-direction are also significantly larger than those in Z-direction. This implies the Y-direction is the main load-carrying direction. The assumption made beforehand on limited displacement proved to be correct, justifying the one-way coupled approach.

4   Simplified design method

The method currently adopted in this research proved to work. The 3D aspect of the model is required to properly capture the structural behaviour and stress distribution in the structure, whereas, a 2D model would assume the walls as cantilevering beams and thus misleading results. A 2D model would however be much more efficient and faster. Based on characteristics found in the 3D analysis of the structural behaviour, a new preliminary design method is proposed in this section, working towards an equivalent 2D model.

4.1 Finding bending moments

Several aspects lead to the suspicion that the main walls of the OWC behave like beams in the Y-direction. As stated, this is the direction which carries the majority of the load. Looking at the wall geometries, they all are taller than they are wide. Besides, they are rigidly constrained at both sides. At the vertical ends, there mostly is only one constraint. The back wall is connected at both vertical ends, but the top part is still free to move back and forth. The idea of beam-like behaviour is further investigated here. From basic mechanics principles, the bending moment distribution in a clamped beam under a constant load is known. The maximum bending moment occurs at the constraint with a magnitude of $ql^2/12$, where q is the load and l is the span. The governing forces in Y-direction indeed were found at the constraints. By substituting the net pressure along a wall and the wall width in the formula, the bending moment can be calculated in another way. A comparison between the two shows to what extent the approximation is correct.
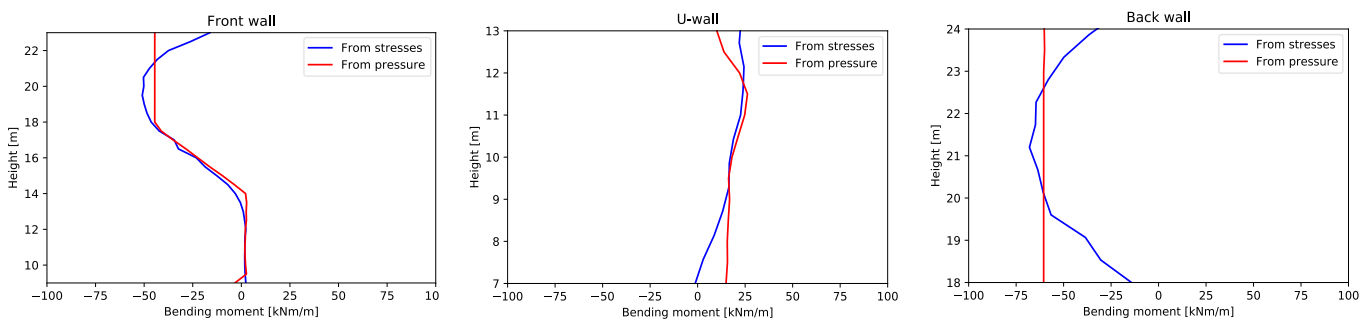

Figure 13: Comparison of bending moments calculated through different methods for the front wall (left), U-wall (middle) and back wall (right).

Figure 13 contains the plots for the three walls, showing the bending moment calculated using both methods. Although only a single moment in time is presented, the result is representative for the full set of data. Both methods show very similar behaviour, both in magnitude and through time. The largest discrepancies occur near the (constrained) boundaries at the top and bottom of the walls. This is where in reality the 3D structural behaviour comes into play, which is properly captured by the numerical structural analysis (red line), but not by the newly proposed method (blue line). The local differences are clearly visible at the top of the front wall, the bottom of the U-wall and both ends at the back wall. However, for design purposes the main interest is focused on extreme values, which are captured relatively well, with differences in the order of magnitude of just few kilonewton meter. The new method was checked by repeating the process for the bending moments at midspan, where the moment is half that of the constraint in magnitude and opposite in sign. This gave very similar results. Bending moments in the walls can thus directly be approximated from the water pressures, which are independent of the structural analysis. This thus removes the need for a structural analysis within the numerical model, reducing the numerical model significantly in size.

4.2 From 3D to 2D

The approximation method for finding the bending moments reduces the urgency of a structural analysis. For a next step, a look is taken at the flow velocity profiles of water inside the OWC. These are expected to be predominantly 2D, where the flow is constant along the transverse direction. The assumption of constant load along the transverse direction is mainly supported by the relatively short width of the chamber. Indeed, the chamber width being only 3.87 m the apparent wave length (even in the case of short crested waves) at the interface between the water surface and the frontal wall of the structure would always be several times larger than the chamber width, then generating a constant pressure along the transverse direction. In passing, note that this fact was highlighted by Malara et al. (2017) within the framework of the linear potential theory. Specifically, they showed that directionality affects marginally distribution and magnitude of the wave pressure exciting the water column and, thus, the U-OWC water column displacement. With the 3D model, this can be verified. Grids of data points were placed at three cross sections in the device: the front duct (horizontal),

below the front wall (vertical) and the main chamber (horizontal). Here, the flow velocity perpendicular to the grid-plane is measured during the oscillation cycles. Results are showcased in Figure 14, where the top row is at peak inflow and the bottom row at peak outflow. Indeed, it is observed the flow is predominantly constant over the transverse width, especially near the walls.
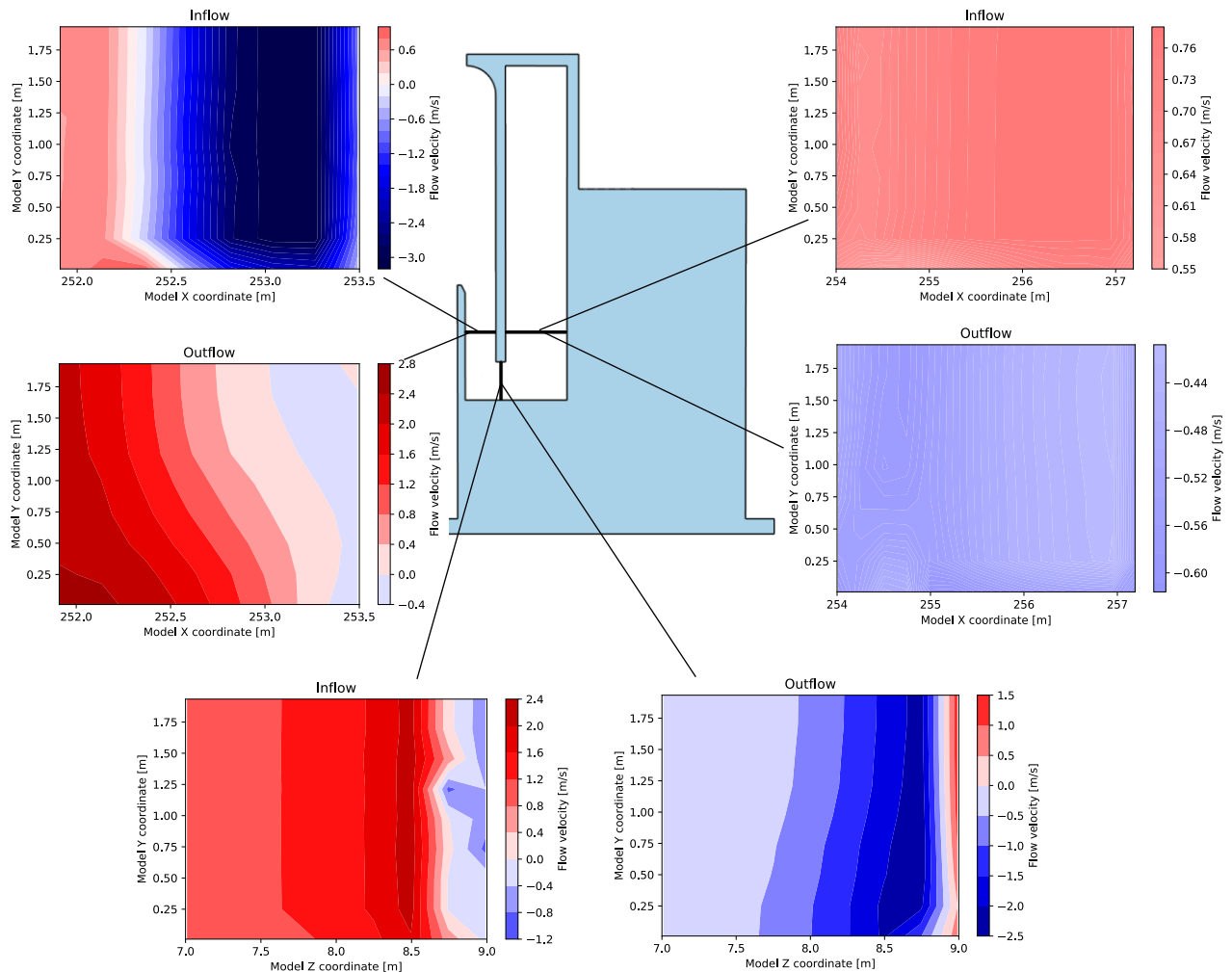

Figure 14: Flow velocity profile in the duct, below the front wall and in the chamber during maximum inflow and maximum outflow.

With this new information, one could go even further with the new design method. The main reasoning for a 3D model was to accurately capture the structural behaviour and find the correct design forces. This structural analysis has now become redundant due to the presented results and methodology, as bending moments are found directly from the pressures with similar accuracy. The proposed method also relies on the assumption of a constant pressure along the transverse width. Based on the 2D flow pattern in the device, it can be argued that this is indeed the case. This was also further confirmed by assessing the pressures in the simulation. The pressures required for finding the bending moments then have only to be known along a single vertical line, implying a 2D model would be sufficient as long as the 3D hydrodynamic behaviour is simulated accordingly and a structural domain is absent.

5 Conclusion

The breakwater integrated oscillating water column device is seen as a promising technique of extracting energy from water waves. The main problem is that the costs are still too high to compete with common renewable sources such as wind and solar energy. The proposed method of cost reduction is through structural optimisation. The possibilities for

this unusual approach in this field were investigated with the device in Civitavecchia used as a case study. A numerical study was set up, coupling CFD to a structural analysis. This allowed it to directly obtain the stresses in the structure caused by wave impact. The model performed well, but assumptions made still leave room for improved accuracy.

It was found approximately 35% of the concrete can be saved among the three main transverse walls. This result is directly related to the case of Civitavecchia. It may only be seen as a sign of potential optimisation for other designs. In the process, the energetic performance under operational conditions was monitored. This was only done based on one adopted sea state and therefore gives a limited view. The actual geometry of Civitavecchia performed best, however, one of the geometrical variations, although having a lower energetic performance than the current geometry of Civitavecchia, showed a significantly larger structural optimisation potential.

Further investigation was done in order to describe the structural behaviour of the device with the overall goal of getting better insight in its response under extreme wave loading and therefore propose a simpler design process. For a set of geometrical changes, the governing load cases were found. These were linked to their position in the wall and moment of occurrence with respect to the oscillation within the internal chamber. For each of the three investigated structural components, it is now known where and when to expect critical loading conditions. Geometrical changes hardly had any effect on the behavioural properties making the description of the structural behaviour valid beyond the reference case.

Based on the results found in the structural behavioural analysis, a new and simplified design method was proposed. It was shown that the walls behave like beams from a structural point of view, allowing the calculation of the bending moments directly from the net pressure acting on a wall, applying standard beam theory. Results were promising, as the resulting moments matched quite well with those found from the full numerical structural analysis, making the detailed structural analysis redundant. With water pressures found constant over the transverse width, this opens up to the opportunity to scale down the model toward a 2D simulation, as long as the 2D model can properly capture the 3D hydrodynamic behaviour.

Author contributions

BG: Conceptualisation, modelling, analysis and drafting the paper text. JB: Supervision, text editing, result revision. AA: Conceptualisation, supervision CFD modelling, text editing, result revision. GM: Field case supervision, supervision, text editing, result revision. MH: Supervision FEM modelling, text editing, result revision. HH: Structural aspects supervision, text review.

Notation

Name	Symbol	Unit
Wave height	H	m
Wave period	T	s
Pressure drop	Δp	Pa
Turbine length	L	m
Dynamic viscosity	μ	N/m^{2}s
Inertial damping coefficient	P_i	kg/m^4
Inertial resistance coefficient	R_i	1/m
Viscous damping coefficient	P_v	kg/m^{3}s
Viscous resistance coefficient	R_v	1/m^2
Flow velocity	v	m/s
Air density	ρ_a	kg/m^3
Time step	Δt	s
Cells per wave length	n	$-$
Acting bending moment	M_{Ed}	Nm
Acting normal force	N_{Ed}	N
Normal force in concrete	N_c	N
Wall thickness	h	m
Concrete compression zone height	x_u	m
Concrete characteristic compressive strength	f_{ck}	N/mm^2
Concrete design compressive strength	f_{cd}	N/mm^2
Concrete shear capacity	$v_{Rd,c}$	N/mm^2
Reinforcement ratio	ρ_s	$-$
Reinforcement tensile strength	f_{yd}	N/mm^2

References

Arena, F., Romolo, A., Malara, G. and Ascanelli, A., 2013. On Design and Building of a U-OWC Wave Energy Converter in the Mediterranean Sea: A Case Study. Proceedings of the ASME 2013 32nd International Conference on Ocean, Offshore and Arctic Engineering. Volume 8: Ocean Renewable Energy, Nantes, France. June 9–14.

Arena, F., Romolo, A., Malara, G., Fiamma, V. and Laface, V., 2017. The First Full Operative U-OWC Plants in the Port of Civitavecchia. Proceedings of the ASME 2017 36th International Conference on Ocean, Offshore and Arctic Engineering. Volume 10: Ocean Renewable Energy, Trondheim, Norway. June 25-30.

Ashlin, S.J., Sannasiraj, S.A. and Sundar, V., 2015. Wave Forces on an Oscillating Water Column Device. Procedia Engineering, 116: 1019-1026.

Ashlin, S.J., Sundar, V. and Sannasiraj, S.A., 2017. Pressures and Forces on an Oscillating Water Column–Type Wave Energy Caisson Breakwater. Journal of Waterway, Port, Coastal, and Ocean Engineering, 143(5): 04017020.

Boccotti, P., 2007a. Caisson breakwaters embodying an OWC with a small opening—Part I: Theory. Ocean Engineering, 34: 806-819.

Boccotti, P., 2007b. Comparison between a U-OWC and a conventional OWC. Ocean Engineering, 34: 799-805.

Bruce, T. and O'Callaghan, J., 2013. Oscillating water column wave energy converters at the coast: A review and forward look, Coastal Structures 2011, pp. 345-356.

Bull, D. and Ochs, M.E., 2013. Technological Cost-Reduction Pathways for Oscillating Water Column Wave Energy Converters in the Marine Hydrokinetic Environment. SANDIA Report: SAND2013-7205.

Castellino, M., Romano, A., Lara, J.L., Losada, I.J. and De Girolamo, P., 2021. Confined-crest impact: Forces dimensional analysis and extension of the Goda's formulae to recurved parapets. Coastal Engineering, 163: 103814.

Castellino, M., Sammarco, P., Romano, A., Martinelli, L., Ruol, P., Franco, L. and De Girolamo, P., 2018. Large impulsive forces on recurved parapets under non-breaking waves. A numerical study. Coastal Engineering, 136: 1-15.

Dermentzoglou, D., Castellino, M., De Girolamo, P., Partovi, M., Schreppers, G.-J. and Antonini, A., 2021. Crownwall Failure Analysis through Finite Element Method. Journal of Marine Science and Engineering, 9(1): 35.

Falcão, A.F.O. and Henriques, J.C.C., 2016. Oscillating-water-column wave energy converters and air turbines: A review. Renewable Energy, 85: 1391-1424.

Fenton, J.D., 1985. A Fifth-Order Stokes Theory for Steady Waves. Journal of Waterway, Port, Coastal, and Ocean Engineering, 111: 216-234.

Goda, Y., 1974. New Wave Pressure Formulae for Composite Breakwaters. Coastal Engineering 1974. jun.

Goda, Y., 2000. Random Seas And Design Of Maritime Structures (2nd Edition). World Scientific.

Gunn, K. and Stock-Williams, C., 2012. Quantifying the global wave power resource. Renewable Energy, 44: 296-304.

Kuo, Y.S., Lin, C.S., Chung, C.Y. and Wang, Y.K., 2015. Wave loading distribution of oscillating water column caisson breakwaters under non-breaking wave forces. Journal of Marine Science and Technology, 23: 78-87.

Magagna, D. and Uihlein, A., 2015. Ocean energy development in Europe: Current status and future perspectives. International Journal of Marine Energy, 11: 84-104.

Malara, G. and Arena, F., 2013. Analytical modelling of an U-Oscillating Water Column and performance in random waves. Renewable Energy, 60: 116-126.

Malara, G., Gomes, R.P.F., Arena, F., Henriques, J.C.C., Gato, L.M.C. and Falcão, A.F.O., 2017. The influence of three-dimensional effects on the performance of U-type oscillating water column wave energy harvesters. Renewable Energy, 111: 506-522.

Mørk, G., Barstow, S., Kabuth, A. and Pontes, M.T., 2010. Assessing the Global Wave Energy Potential. 29th International Conference on Ocean, Offshore and Arctic Engineering: Volume 3.

Naty, S., Viviano, A. and Foti, E., 2016. Wave Energy Exploitation System Integrated in the Coastal Structure of a Mediterranean Port. Sustainability, 8: 1342.

NEA, IEA and OECD, 2015. Projected Costs of Generating Electricity 2015. International Energy Agency, Nuclear Energy Agency, Organisation for Economic Co-operation and Development.

Ning, D.Z., Guo, B.M., Wang, R.Q., Vyzikas, T. and Greaves, D., 2020. Geometrical investigation of a U-shaped oscillating water column wave energy device. Applied Ocean Research, 97: 102105.

OCEAN, S.I., 2013. Ocean Energy: Cost of Energy and Cost Reduction Opportunities, SI OCEAN.

Perić, M., 2017. Best practices for flow simulations with waves. Presentation at Star Global Conference 2017.

Rivero, I.B., 2018. Investigation of the robustness of an oscillating water column breakwater under extreme wave conditions. MSc Thesis, Delft University of Technology.

Scarpetta, F., Gurnari, L., Torresi, M., Filianoti, P. and Camporeale, S., 2017. A CFD simulation of a full-scale U-OWC breakwater. Proceedings of the 12th European Wave and Tidal Energy Conference.

Scialò, A., Henriques, J.C.C., Malara, G., Falcão, A.F.O., Gato, L.M.C. and Arena, F., 2021. Power take-off selection for a fixed U-OWC wave power plant in the Mediterranean Sea: The case of Roccella Jonica. Energy, 215: 119085.

SIEMENS, 2019. Simcenter STAR-CCM+ Documentation. SIEMENS.

Vicinanza, D., Lauro, E.D., Contestabile, P., Gisonni, C., Lara, J.L. and Losada, I.J., 2019. Review of Innovative Harbor Breakwaters for Wave-Energy Conversion. Journal of Waterway, Port, Coastal, and Ocean Engineering, 145: 03119001.

WEC, 2016. World Energy Resources 2016, World Energy Council.